Numerical simulation and modeling of ice shedding: Process initiation

Lokman Bennani, Philippe Villedieu, Michel Salaün, Pierre Trontin

Numerical simulation and modeling of ice shedding: Process initiation

L. Bennani [a,b,*], P. Villedieu [b], M. Salaun [c], P. Trontin [b]

[a] Airbus Operations SAS, 316 Route de Bayonne, 31060 Toulouse, France
[b] ONERA DMAE-MH, 2 avenue Edouard Belin, 31000 Toulouse, France
[c] ISAE, 10 avenue Edouard Belin, 31000 Toulouse, France

ARTICLE INFO

Keywords:
Icing
Ice shedding
Ice protection
Electro-thermal
Fracture mechanics
Damage mechanics

ABSTRACT

In aeronautics, the issue of ice shedding prediction is of prime importance in the assessment of electro-thermal ice protection systems. In this paper, an ice shedding mechanism based on pressure redistribution in the water film formed at the ice/airfoil interface is proposed. This pressure distribution induces a stress concentration that leads to crack propagation in the ice. To determine whether this mechanism is relevant or not, two numerical experiments are performed. The results of these numerical experiments and the influence of a few material parameters are discussed, as well as their limitations and possible consequences arising from some of the hypotheses.

The numerical modeling is based on recent works on damage/fracture mechanics which provide a general framework for fracture mechanics computation. The effects of numerical parameters and mesh size are discussed. A mixed mode test case based on experimental data is also performed. This test case had not been attempted before on this particular numerical method, which therefore serves as further validation.

1. Introduction

In typical flight icing conditions, the water droplets contained in clouds are in a supercooled state. When an aircraft encounters such conditions, those droplets freeze upon impacting its surface, therefore leading to ice build-up. In the aeronautical world, icing is one of the most serious threats that can be encountered. Not only does it increase mass but it may also lead to a degradation of aerodynamic performances, blocked air intakes (among other undesirable consequences).

Aircraft manufacturers must therefore comply with certifications and regulations regarding flight safety in icing conditions. In order to achieve that goal, several ice protection technologies may be used. One commonly used is the "bleed-air" system: hot air is taken from the engines and blown onto the protected surface, as shown in Fig. 1.

However, this system is energy-greedy, and in the context of "more electric" aircraft and reduction of fuel consumption, new systems are being investigated. One of these systems is the electro-thermal ice protection system (ETIPS). This system is composed of heater mats installed within a multi-layered material and can be used in anti-icing or deicing configurations [2,3].

The nominal functioning of an ETIPS in de-icing mode is as follows (illustrated in Fig. 2): A region called the parting strip, usually located around the leading edge (for example the region corresponding to heater C), is constantly protected from ice accretion. More precisely, the corresponding heater mat is in anti-icing mode. The other heaters are activated according to a given cycle. Thus ice accretion is permitted in regions other than the parting strip. When a heater mat is activated, it melts a part of the ice in contact with the surface, creating a liquid water film and therefore lowering ability of the ice block to adhere to the surface. The aerodynamic forces are then able to detach the ice block (or part of it) from the surface.

In order to assess the performance of such a system, it is essential to understand the mechanisms by which the aerodynamic forces manage to detach the ice. The current state of the art in icing codes is an empirical criterion. It states that, if the length of the liquid water film has a sufficient length (typically 80% of the whole contact length), then the ice block detaches [2]. However such an empirical criterion is unsatisfactory. Therefore, to obtain more physical ice shedding models, a better understanding of the detachment process is needed.

In this paper a mechanism that could play a crucial role in the process of detachment of the ice block (from the protected surface)

* Corresponding author at: Airbus Operations SAS, 316 Route de Bayonne, 31060 Toulouse, France.

E-mail addresses: lokman.bennani@airbus.com (L. Bennani), philippe.villedieu@onera.fr (P. Villedieu), m.salaun@isae.fr (M. Salaun), pierre.trontin@onera.fr (P. Trontin).

Nomenclature

α	angle of attack (°)
ϵ	strain
λ, μ	Lamé coefficients (Pa)
$\mathcal{H}$	history function (J m^{-3})
ν	Poisson's ratio
ϕ	porosity
d	damage variable
d_{grain}	grain size (m)
E	Young's modulus (Pa)
E_{crack}	crack energy (J)
E_{el}	elastic energy (J)
g_c	energy release rate (J m^{-2})
h	mesh element characteristic size (m)
h_{fp}	thickness of the flat plate (m)
K_{IC}	fracture toughness (Pa $\sqrt{\text{m}}$)
L_{fp}	length of the flat plate (m)
L_f	length of melted region between ice and protected surface (m)
L_t	total contact length between ice and protected surface (m)
P_∞	freestream pressure (Pa)
P_c	contact point between melted region and airflow (m)
$p_{exterior}$	exterior pressure distribution (Pa)
$p_{redistributed}$	redistributed pressure (Pa)
T	temperature (K or °C)
T_∞	freestream static temperature (K)
u	displacement (m)

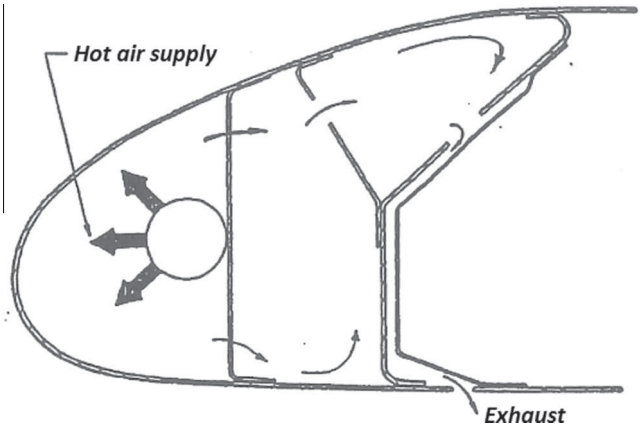

Fig. 1. Illustration of a bleed air system [1].

is presented. First, the proposed detachment mechanism is presented. Then, the modeling and numerical techniques used in this study are introduced. This will be followed by a parameter identification and validation against experimental data. After that numerical experiments are presented and performed. Finally the results are discussed.

2. Proposed mechanism

Let us consider a situation as depicted Fig. 3, where ice has accreted just after the parting strip. The contact zone between the ice and the surface extends over a curvilinear distance, say L_t. The proposed mechanism is based on two observations. Firstly, the flow over such a shape will induce pressure variations over the lump. Fig. 4 depicts a typical pressure distribution. Secondly, due to the ETIPS, a certain amount of ice in contact with the surface has melted. This leads to the creation of a thin film of liquid water extending over a distance L_f. A contact point, P_c, exists between the external flow and the film. The pressure at this point will be entirely redistributed by the film over the length L_f due to the absence of motion in the liquid water film[1] (hydrostatic pressure equilibrium). The presence of the ice shape will cause an acceleration of the flow when passing over it, which decreases pressure at the same time. This means the pressure recovered in the film will be higher than that acting on the external surface.

This pressure distribution creates a lifting force. To this force, one has to add the viscous forces, which are tangential. Thanks to these forces several outcomes may be possible:

- The whole length is melted ($L_f = L_t$) in which case the ice no longer adheres to the surface (or only by means of surface tension effects).
- *Adhesive break*: part of the length $L_f = x\%L_t$ is melted and the adhesion forces that maintain ice on the surface are no longer strong enough.
- *Brittle failure*: part of the length $L_f = x\%L_t$ is melted, ice can still adhere, but a crack may nucleate due to stress concentration and propagate through the ice, therefore tearing off a part of it.
- *Cohesive break*: part of the length $L_f = x\%L_t$ is melted, ice can still adhere, but a crack may nucleate due to stress concentration and propagate along the ice/protected surface interface.
- Ice shedding is due to a combination of the above possibilities.

The mechanisms leading to ice shedding are to this day not well understood. Experimental observation shows that brittle failure plays a crucial role. Hence, as a first approach to the problem, the present study is confined to the third possibility presented above, concerning brittle failure. To do so, a crack nucleation and propagation model is required. This implies knowledge about the mechanical properties of atmospheric ice.

3. Properties of atmospheric ice

One of the main problems that arises is to determine what mechanical properties are going to be used in order to characterize atmospheric ice. Unfortunately, very few studies on the subject exist. Most studies are interested in the tensile or compressive strength but do not provide many information on mechanical characteristics in the form of well defined laws [4–6]. These experiments are very difficult to conduct due to the vast number of parameters on which those properties depend, making the issue all the more complicated. For example, Eskandarian [7] reports a determination of Young's modulus and Poisson's ratio for porous ice.

Therefore, as a first approach, data and empirical laws given by experiments for natural ice are used as a starting point. These laws are more precise, and more widely studied. Nevertheless, they

[1] In fact, as liquid water takes up less volume than ice, a gap may form in the melted region. That is to say, the water film may not entirely occupy the volume formerly made out of ice and air may be allowed to fill in the gap. However, we would still be in a case of hydrostatic pressure equilibrium. Therefore pressure redistribution would still occur as described.

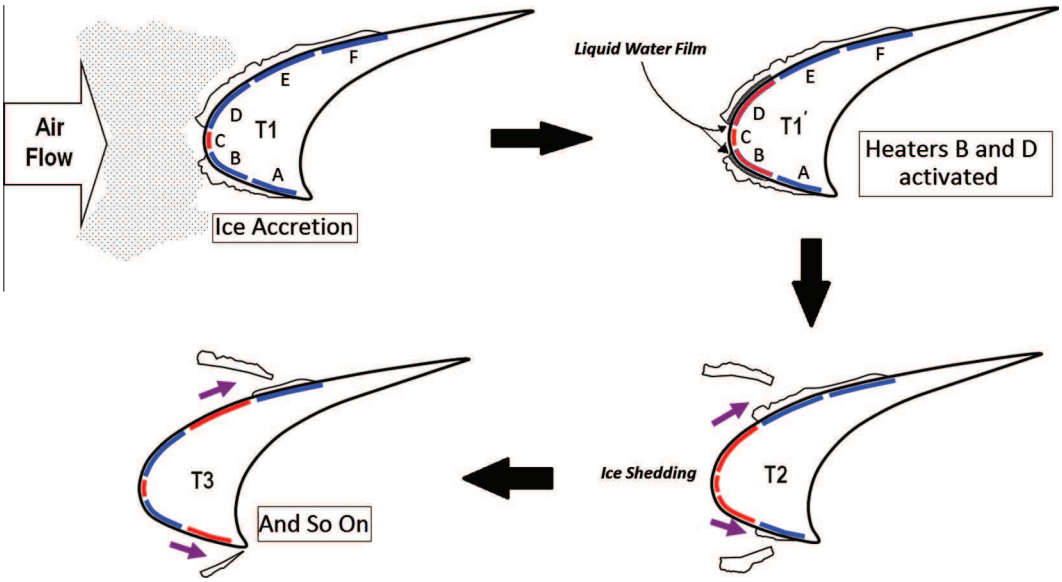

Fig. 2. Operating of an ETIPS.

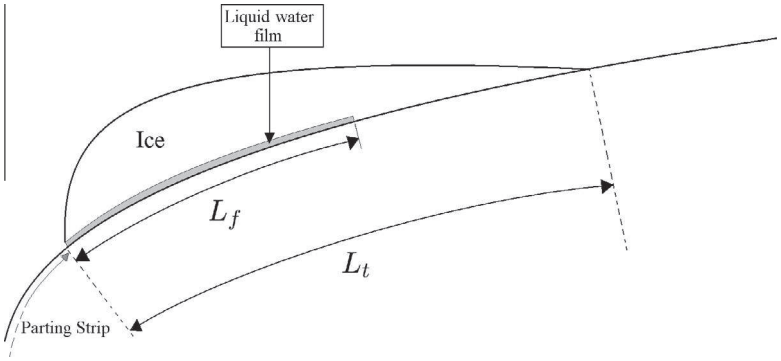

Fig. 3. Accreted ice and water film – geometric parameters.

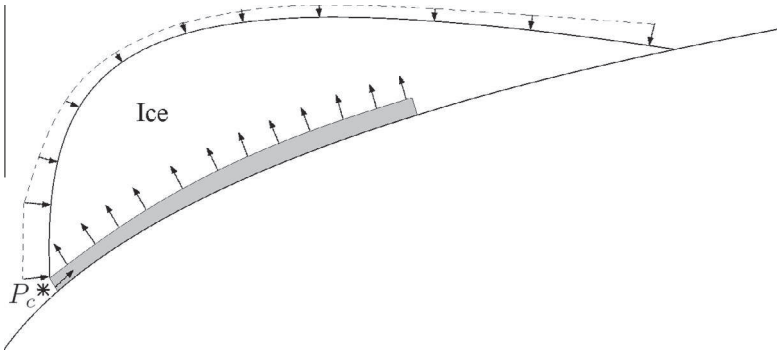

Fig. 4. Schematic pressure distribution on ice lump.

apply to different types of ice (natural, polycrystalline, sea water). As such, they do not apply to atmospheric ice. Therefore only the general form of the empirical laws is retained. In Section 6 their parameters will be identified so as to fit experimental data for atmospheric ice.

According to Schulson and Duval [8], the most precise results for the elastic constants were obtained by Gammon et al. [9]. In the case of a homogeneous polycrystalline ice aggregate, it may be assumed that the grains (crystallites) are oriented randomly making it elastically isotropic. The parameters characterizing homogeneous isotropic elastic behavior of polycrystalline ice are given in the following Table 1 [8,9]:

The temperature dependence of Young's modulus is obtained using the formula (1), given in [8]:

$$E(T) = E(T_r)[1 - a(T - T_r)] \tag{1}$$

Table 1
Elastic constants of interest for isotropic polycrystalline ice at $T = -16\ ^\circ C$.

Young's modulus, E	9.33×10^9 Pa
Poisson's ratio, ν	0.325

where $a = 1.42 \times 10^{-3}\ K^{-1}$ and T_r is the temperature at which the initial measurement was conducted.

Grain size (d_{grain}) and porosity (ϕ) also affect the material parameters. Their values depend on the way the ice was formed. Effects of porosity on Young's modulus are taken into account by combining relation (1) with the empirical law: $E = E_0 - b\phi$ [8]. For fracture toughness, two empirical laws, $K^*_{I0} = \left[K_{I0} + \frac{\gamma}{\sqrt{d_{grain}}} 10^{-1.5}\right]$ and $K_{IC} = K^*_{I0}(1.0 - c\phi)$ [8], are combined to give:

$$E = E(T_r)[1 - a(T - T_r)] - b\phi \quad \phi \leqslant 0.1 \quad \text{and E is in GPa} \tag{2}$$

$$K_{IC} = \left[K_{I0} + \frac{\gamma}{\sqrt{d_{grain}}} 10^{-1.5}\right](1.0 - c\phi) \quad \text{with } d_{grain} \text{ in meters} \tag{3}$$

where $b = 35.1$ GPa, $c = 1.0$, $K_{I0} = 58.3$ kPa $\sqrt{\text{m}}$ and $\gamma = 42.4$ kPa m. K_{IC} is the fracture toughness (the critical stress intensity factor). It may be linked to the crack energy release rate with the relations:

$$g_c = (1 - \nu^2)\frac{K_{IC}^2}{E} \quad \text{for plane strain} \tag{4}$$

$$g_c = \frac{K_{IC}^2}{E} \quad \text{for plane stress} \tag{5}$$

Moreover, according to Lui and Miller [10] the ambiant temperature also has an effect on fracture toughness. The results of their measurements are shown in Fig. 5.

As a first approximation this effect can be taken into account with a linear relation which may be integrated into (3) in two ways:

$$\text{Law 1}: \ K_{IC} = \left[K_{I0} - c_T(T - 273.15) + \frac{\gamma}{\sqrt{d_{grain}}} 10^{-1.5}\right](1.0 - c\phi) \tag{6a}$$

$$\text{Law 2}: \ K_{IC} = \left[K_{I0} + \frac{\gamma}{\sqrt{d_{grain}}} 10^{-1.5}\right](1.0 - c\phi) - c_T(T - 273.15) \tag{6b}$$

where c_T is a parameter which will be identified, and $T < 273.15$ K.

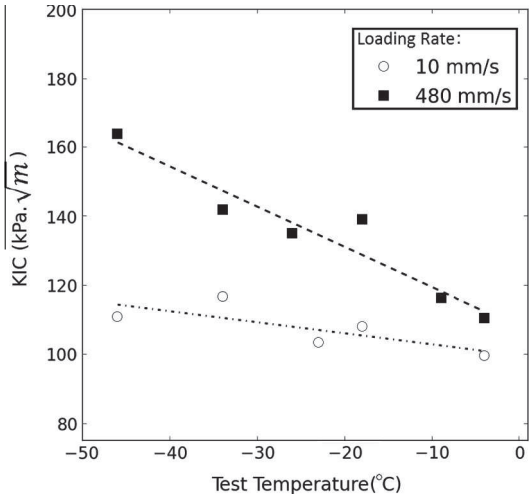

Fig. 5. Effect of testing temperature on fracture toughness at different loading rates [10].

4. Fracture modeling method

Modeling techniques based on continuum mechanics have already been applied to ice. Scavuzzo et al. performed a finite element analysis of the stress distribution due to aerodynamic forces in an accreted ice block [11]. More recently, Zhang et al. have used a crack propagation and re-meshing technique to study ice break up [12]. However these studies did not take into account the effect of an ice protection system.

Here we choose to use a method close to those of continuum damage mechanics. In the following paragraph we construct our model by adapting the approach adopted by Miehe et al. [13] to a stationary case. The idea is to introduce a parameter d that characterizes the local state of damage/fracture [14] in the ice block. The starting point is a principle of conservation of energy [15] whose physical motivation is the following: When a solid is deformed by action of external forces, it internally stores elastic deformation energy. If, locally, this energy exceeds a certain critical energy then it will cause an increase in crack surface. Therefore, if a crack nucleates and/or propagates, a possible mechanism (from a macroscopic point of view) is a process of energy transfer from the applied forces to elastic deformation energy, which in turn may be transformed into crack surface energy. Fig. 6 illustrates this transfer from elastic to crack energy.

The main input parameters required for the model are a crack surface energy (8) and an elastic energy (12). Let $\psi(\epsilon, d)$ be the elastic strain energy per unit volume, and $\phi(d, \nabla d)$ be the fracture energy per unit volume. $\epsilon = \frac{1}{2}(\nabla u + (\nabla u)^T)$ is the strain and u the displacement field. Therefore the total elastic energy will be $E_{el} = \int_\Omega \psi(\epsilon, d) dV$ and the total crack energy will be $E_{crack} = \int_\Omega \phi(d, \nabla d) dV$. When external forces are applied, the change in energy is equal to the work produced by those forces. Thus we have:

$$\delta E_{crack} + \delta E_{el} = \int_\Omega f_{vol} \delta u \, dV + \int_{\Gamma_1} f_{surf} \delta u \, d\Gamma \tag{7}$$

where f_{vol} is a volume force, Γ_1 is a part of the boundary $\partial\Omega = \Gamma_1 \cup \Gamma_2$ where a surface force f_{surf} is applied. Γ_2 is the part of the boundary where a displacement u_d is imposed.

The crack energy is obtained by using a regularized crack energy functional given by Bourdin et al. [16].

$$E_{crack} = \int_\Omega \phi(d, \nabla d) dV = \int_\Omega g_c \left[\frac{1}{2l} d^2 + \frac{l}{2} \nabla d \cdot \nabla d\right] dV \tag{8}$$

where g_c is the crack energy release rate, the damage variable d lies between 0 and 1 ($d(x) = 0$ corresponding to an undamaged state and $d(x) = 1$ to a fractured state).

The term $\frac{1}{2l} d^2 + \frac{l}{2} \nabla d \cdot \nabla d$ can be interpreted as a regularized approximation of the Dirac δ-function related to the crack surface. l is an adjustable parameter that controls the width of the regularized crack. From a minimization of surface energy view point, the regularization involves an interplay between $\frac{1}{2l} d^2$ which tends to localize and $\frac{l}{2} \nabla d \cdot \nabla d$ which tends to spread. The elastic energy density will be defined in more detail further.

By using variational arguments it can be shown that (9):

$$\begin{aligned} &\sigma = \frac{\partial \psi}{\partial \epsilon} \quad \text{in } \Omega \\ &\frac{g_c}{l} d - g_c l \triangle d = -\frac{\partial \psi}{\partial d} \quad \text{in } \Omega \\ &\nabla d \cdot n = 0 \quad \text{on } \partial\Omega \end{aligned} \tag{9}$$

The stress tensor σ is deduced from the choice of ψ. In the case of a linear homogeneous isotropic elastic material, the elastic energy is given by: $\psi(\epsilon) = \frac{\lambda}{2} tr(\epsilon)^2 + \mu tr(\epsilon^2)$. However, considering $-\frac{\partial \psi}{\partial d}$ is the source term, the driving force of the fracture process, ψ must also be chosen according to what part of the elastic

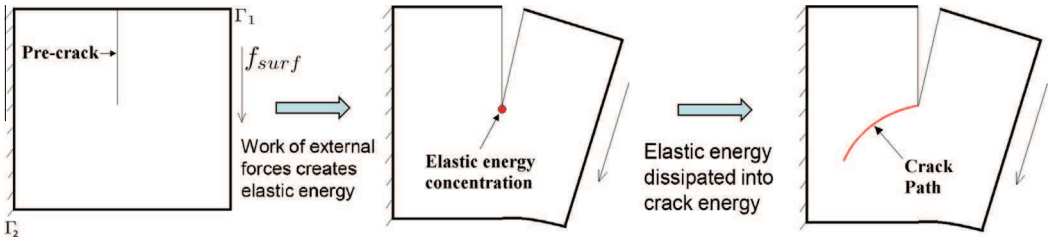

Fig. 6. Energy transfer in crack opening mode.

deformation energy creates or propagates a crack. It is considered that in the case of brittle fracture, only the tensile energy interacts with crack propagation. Thus the elastic energy is split into purely tensile and compressive parts defined by using the eigenvalues of ϵ (ϵ_1 and ϵ_2 in two dimension) and a positive/negative part function noted $\langle\cdot\rangle_\pm$:

$$\psi_0^+(\epsilon) = \frac{\lambda}{2}\langle\epsilon_1+\epsilon_2\rangle_+^2 + \mu(\langle\epsilon_1\rangle_+^2 + \langle\epsilon_2\rangle_+^2) \tag{10}$$

$$\psi_0^-(\epsilon) = \frac{\lambda}{2}\langle\epsilon_1+\epsilon_2\rangle_-^2 + \mu(\langle\epsilon_1\rangle_-^2 + \langle\epsilon_2\rangle_-^2) \tag{11}$$

ψ_0^+ and ψ_0^- represent respectively the undamaged tensile and compressive elastic energies. As stated before, only tensile energy interacts with crack propagation. Thus only $\psi_0^+(\epsilon)$, the tensile part, is multiplied by a function of d, say $f(d)$. The function $f(d)$ represents the degradation of tensile energy due to crack formation and is chosen accordingly:

$$E_{el} = \int_\Omega [f(d)\psi_0^+(\epsilon) + \psi_0^-(\epsilon)]dV \tag{12}$$

Therefore f is a nonincreasing function, $f(0)=1$ and $f(1)=0$. Moreover, when $d=1$ it is asked that the driving force $-\frac{\partial\psi}{\partial d} = -f\prime(d)\psi_0^+(\epsilon)$ be equal to 0. To do so the additional condition $f\prime(1)=0$ is imposed. Under these conditions Miehe et al. [13] proposed the function $f(d)=(1-d)^2$. Using these new relations the complete set of equations becomes:

$$\begin{aligned}
&-div(\sigma(u,d)) = f_{vol} \quad \text{in } \Omega\\
&\sigma\cdot n = f_{surf} \quad \text{on } \Gamma_1\\
&u = u_d \quad \text{on } \Gamma_2\\
&\frac{g_c}{l}d - g_c l\triangle d = 2(1-d)\psi_0^+(\epsilon) \quad \text{in } \Omega\\
&\nabla d\cdot n = 0 \quad \text{on } \partial\Omega
\end{aligned} \tag{13}$$

Eqs. (13) are nonlinear and describe a stationary damaged equilibrium state compatible with the external constraints. They translate conservation of energy. In order to incorporate the irreversible aspect of crack propagation, Miehe et al. [13] introduce a history function $\mathcal{H}$. They propose the following kind of iterative algorithm, which we have implemented using a finite element method:

- Compute the history field:

$$\mathcal{H}^i = max(\mathcal{H}^{i-1}, \psi_0^+(\epsilon^{i-1})) \tag{14}$$

- Compute the damage field:

$$\frac{g_c}{l}d^i - g_c l\triangle d^i = 2(1-d^i)\mathcal{H}^i \quad \text{in } \Omega \tag{15}$$

$$\nabla d^i\cdot n = 0 \quad \text{on } \partial\Omega \tag{16}$$

- Compute the displacement field:

$$-div(\sigma^i(\epsilon^i, d^i)) = f_{vol} \quad \text{in } \Omega \tag{17}$$

$$\sigma^i\cdot n = f_{surf} \quad \text{on } \Gamma_1 \tag{18}$$

$$u^i = u_d \quad \text{on } \Gamma_2 \tag{19}$$

This algorithm can be interpreted as follows. Let's assume a first purely elastic computation has been realized as an initialisation. The locally available tensile energy may then be computed. This energy then becomes a source term for the damage equation. The evolution of damage then changes the way the material deforms. The new deformed state is obtained by solving the equilibrium equation, which in turn gives us a new tensile energy, and so on.

However, it is not exactly the tensile energy that is used to define the source term for the damage equation. Rather, it is a history function noted $\mathcal{H}$. If we consider the iterative process as pseudo-unsteady, the use of the history function can be interpreted in the following manner: At a given iteration i the tensile energy could locally be inferior to its value at iteration $i-1$. Thus if, at a given iteration $d=1$, nothing is preventing it from decreasing at any following iteration. But, clearly in our case, the problem of crack propagation is irreversible: d should not be allowed to decrease. Thus the history function $\mathcal{H}$ aims at taking into account the irreversibility of the crack propagation process. It records, locally, the maximum of the tensile energy over all iterations. This history function then becomes a source term for the equation that governs the evolution of damage. Intuitively, if at a given iteration there was enough tensile energy to increase the damage variable d, then this information will be contained in $\mathcal{H}$ for the following iteration. Nevertheless further investigation remains to be done in order to determine the relevance of this pseudo-unsteady interpretation.

The main advantage of this method is that it does not require an initial crack. On the other hand it should be noted that the main drawback is the need of a refined mesh. Especially in the case of imposed boundary load, the crack tends to spread if the mesh is not refined enough.

5. Model assessment

Now that the modeling strategy is established, it is interesting to perform preliminary checks in order to assess its performance. To do so, the effects of mesh size and spreading length l will first be studied. Secondly, numerical predictions and experimental data will be compared to see how the model performs. Due to the lack of experimental data on atmospheric ice, an experimental test case performed on concrete is reproduced [17].

All computations in this section will be based on the same generic test case (see Fig. 7). It consists of a square specimen (200 mm $\times$ 200 mm) of plain concrete submitted to mixed mode loading, shear and axial at the same time. The specimen has a thickness of 50 mm which is relatively small compared to the other dimensions, therefore a plane stress formulation is chosen. The material parameters are chosen to be $E = 30$ GPa, $\nu = 0.2$ and $K_{IC} = 1$ MPa m$^{-1/2}$ [17,18].

5.1. Size effects

For the study of size effects two meshes ("coarse": 30,000 elements, and "fine": 65,000 elements) are considered. These meshes

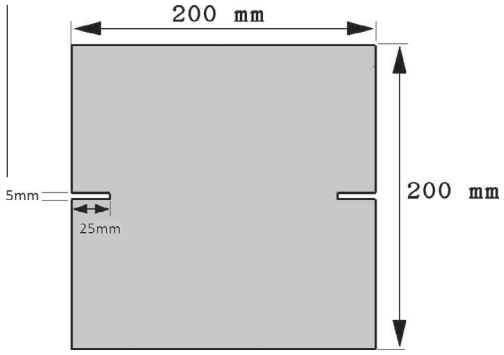

Fig. 7. Generic double edged notch problem illustration.

are designed to have an element characteristic size of respectively $h = 2$ mm and $h = 1$ mm in the region where the crack is expected to propagate. On each mesh two spreading lengths will be investigated, $l = 2$ mm and $l = 5$ mm. A fixed displacement field is imposed at the upper left corner boundary (Γ_u in Fig. 8): $u_x = 20$ µm,$u_y = 25$ µm. A homogeneous Dirichlet boundary condition is applied on $\Gamma_0 : u_x = 0$ m,$u_y = 0$ m.

As can be seen in Figs. 9 and 10, the crack topology for this problem consists of two curved symmetric branches that originate at the notch tips. This topology is typical of this type of double edged mixed mode setup, as presented in the next subsection.

Let's start by taking a look at the effect of the spreading length. Fig. 9 shows the results of two computations realized on the "fine" mesh with $l = 2$ mm and $l = 5$ mm. The crack paths obtained with $l = 5$ mm are clearly more spread out than those obtained with $l = 2$ mm. The crack paths change from one value of l to another, especially near the end of the paths, but this effect is very slight. The same effect is observed on the "coarse" mesh (see Fig. 10).

The effect of mesh size can be seen by comparing Figs. 9(a) and 10(a) for $l = 5$ mm as well as Figs. 9(b) and 10(b) for $l = 2$ mm. For $l = 5$ mm the effect is extremely slight. The same comment can be made for $l = 2$ mm.

The choice of l is not arbitrary, it cannot be chosen too small. For example $l = 0.5$ h yields an irregular solution (see Fig. 11(a)). Choosing $l = 0.25$ h, as shown in Fig. 11(b), completely kills the solution and the crack branches fail to propagate. Thus, this implies good knowledge of the mesh so as to correctly set the spreading length. We join Miehe et al. [13] and consider that a good compromise consists in choosing $l = 2$ h.

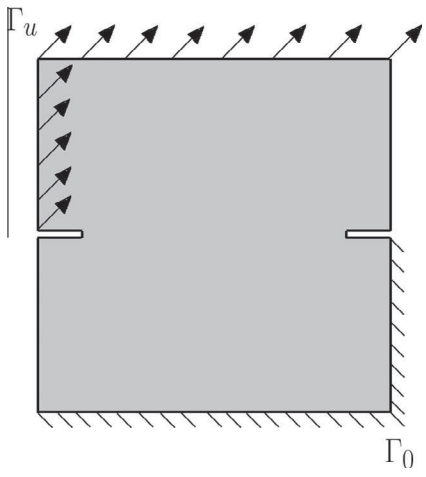

Fig. 8. Double edged notch problem with fixed Dirichlet boundary conditions.

To sum up this section on size effects:

- Reasonably increasing l will spread out the crack but will not significantly change the results. l should not be increased too much so as to maintain a good level of definition for the solution.
- Decreasing l to under-resolved values kills the solution and brings about misleading results.
- For $l \geqslant 2$ h the result will not be significantly mesh sensitive.

5.2. Comparison with experiment

The experimental setup is sketched Fig. 12. To be more precise, the following load path is reproduced: first apply a shear load in displacement control until $Ps = 10$ kN (s axis). Then apply an axial displacement till failure, while maintaining $Ps = 10$ kN with lateral displacement control (t axis).

To the authors knowledge, comparison of this numerical fracture mechanics model with this kind of experiment has not yet been performed. Therefore it also serves as an assessment of the model itself. Numerically this was achieved by imposing displacements at boundaries Γ_{up} and Γ_{down} in the following way:

- Apply displacement u_x and compute Ps.
- Adjust displacement u_x so as to obtain $Ps = 10$ kN.
- Apply displacement u_y until failure.
- Adjust u_x at each iteration to maintain $Ps = 10$ kN while simultaneously enforcing failure with displacement u_y.

Fig. 13 shows the crack paths obtained numerically and the experimental crack paths (respectively at the front and rear faces of the concrete specimen). The crack topology consists of two curved branches each taking their origin at one of the notches. The numerical results match the experimental paths quite well, with a very good agreement for the lower branch. As for the upper branch the model predicts a path that passes slightly lower than the experiment. The crack paths predicted by the model are symmetric with respect to one another. This comes as no surprise given the symmetry of the setup and the hypotheses on the material (linear homogeneous isotropic). This symmetry is not observed for the experimentally obtained crack paths. This very slight difference can be explained by the fact that the concrete specimen is not really homogeneous and isotropic. It consists of a mixture of cement, river gravel and sand among other constituants [17]. Although the aggregates formed by the mixture process are of small size compared to the dimensions of the specimen (ratio 100 [17]) the resulting material will not be perfectly homogeneous and isotropic. Given the highly nonlinear character of crack propagation it is not surprising to observe slightly unsymmetric crack paths.

6. Parameter identification: experimental test case

As stated Section 3, the parameters defining the mechanical properties of ice have to be redefined. Mohamed et al. have performed experiments in order to characterize the tensile strength of atmospheric ice [6]. We reproduce here these experiments and evaluate the tensile strength given by the damage mechanics model. This will serve to assess the applicability of this method to more complex situations and the suitability of the chosen mechanical properties. The goal here is not to provide extremely precise laws. They serve to give a good enough framework so as to confidently interpret the results that will come out of the numerical experiments.

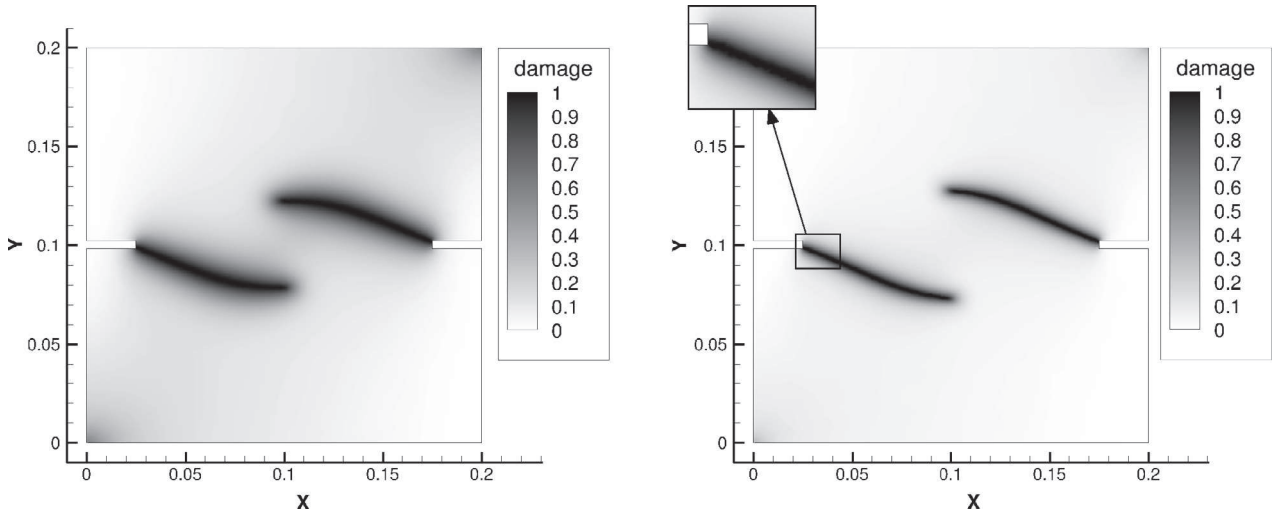

(a) $l = 5h = 5mm$ (b) $l = 2h = 2mm$

Fig. 9. "Fine" mesh computation; $h = 1$ mm.

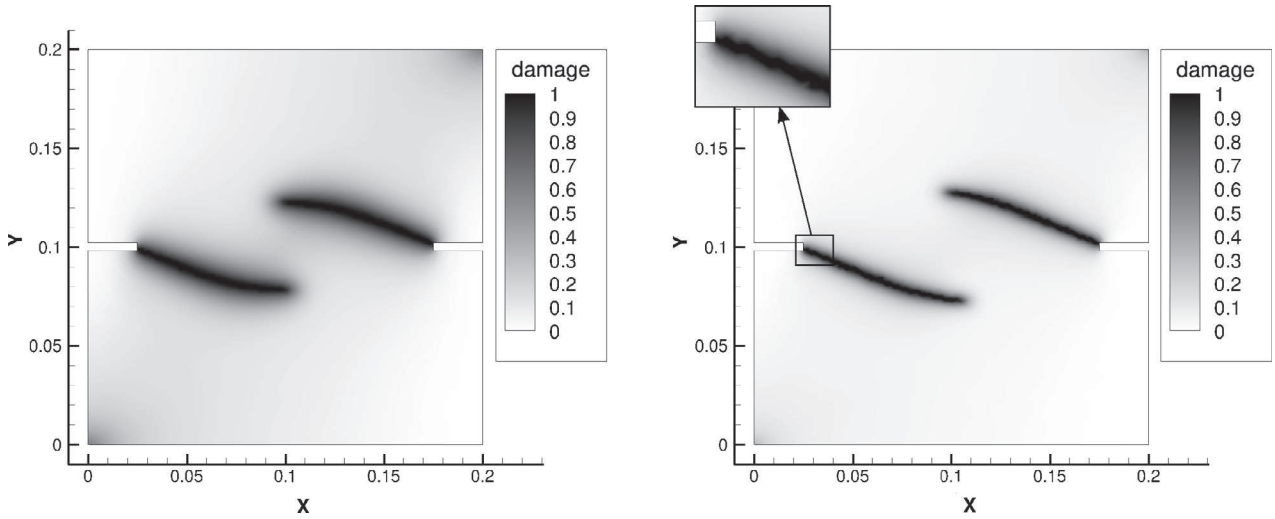

(a) $l = 2.5h = 5mm$ (b) $l = h = 2mm$

Fig. 10. "Coarse" mesh computation; $h = 2$ mm.

The computational domain reproduces the shape of the experimental specimen (minus the region in contact with the elastic holder, via which stress in transmitted to the specimen during the test). It has a dumbell shape with dimensions as shown Fig. 14. All three experimental test temperatures are considered: $-5\,^{\circ}$C, $-10\,^{\circ}$C and $-15\,^{\circ}$C. The accumulation temperature was the same for all samples and set to $-10\,^{\circ}$C. Mohamed et al. report a grain size of 0.7 mm and a porosity of 3%.

If relations (2) and (3) are chosen in their initial form, the model gives a tensile strength of 1.1 MPa for all temperatures. This means tensile strength is underestimated and no test temperature effect is captured. That is why test temperature effect are incorporated through relation ((6)). To sum up, the following relations (law 1 for K_{IC}) are used:

$$E = E(T_r)[1 - a(T - T_r)] - b\phi \quad \phi \leqslant 0.1 \quad \text{and E is in GPa}$$

$$K_{IC} = \left[K_{I0} - c_T(T - 273.15) + \frac{\gamma}{\sqrt{d_{grain}}}10^{-1.5}\right](1.0 - c\phi)$$

with d_{grain} in meters and $T < 273.15$. The values of a and b, which define the law for Young's modulus, are left unchanged: $a = 1.42 \times 10^{-3}$ K^{-1} and $b = 35.1$ GPa. With the law for Young's modulus now fixed, for each temperature, we apply the mean experimental tensile strength and search for the values of K_{IC} that lead to a fractured state. We are then left with the problem of defining a law which will yield these values. As c_T defines the effect of test temperature on K_{IC}, it needs to be redefined. But an identification involving only c_T would yield 3 equations for 1 unknown. Considering the initial relation (3) underestimates tensile strength, a good choice is to also redefine the parameter K_{I0}, which almost acts as an offset value. With all other parameters fixed we are led to the following set of 3 equations for 2 unknowns:

$$\begin{bmatrix} 1 & -(T1 - 273.15) \\ 1 & -(T2 - 273.15) \\ 1 & -(T3 - 273.15) \end{bmatrix} \begin{bmatrix} K_{I0} \\ c_T \end{bmatrix} = \begin{bmatrix} \frac{K_{IC}(T=T1)}{1.0 - c\phi} - \frac{\gamma}{\sqrt{d_{grain}}}10^{-1.5} \\ \frac{K_{IC}(T=T2)}{1.0 - c\phi} - \frac{\gamma}{\sqrt{d_{grain}}}10^{-1.5} \\ \frac{K_{IC}(T=T3)}{1.0 - c\phi} - \frac{\gamma}{\sqrt{d_{grain}}}10^{-1.5} \end{bmatrix}$$

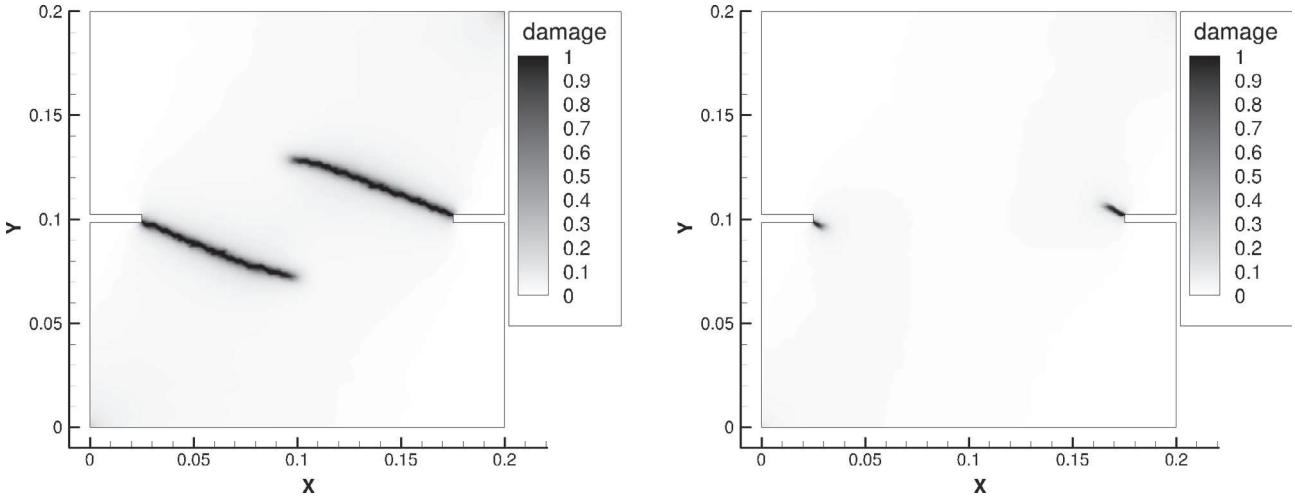

(a) $l = 0.5h = 1mm$ (b) $l = 0.25h = 0.5mm$

Fig. 11. "Coarse" mesh computation with under-resolved l.

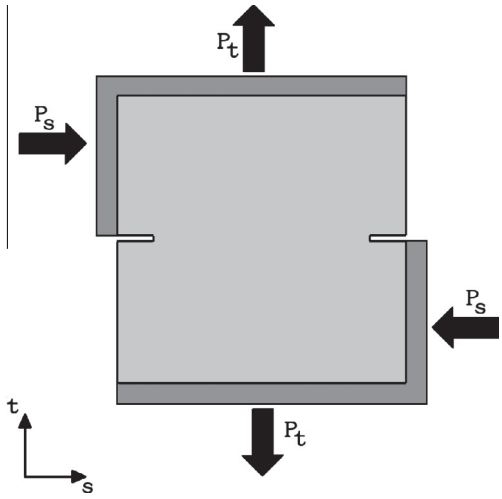

Fig. 12. Double edged notch problem with axial and shear loads.

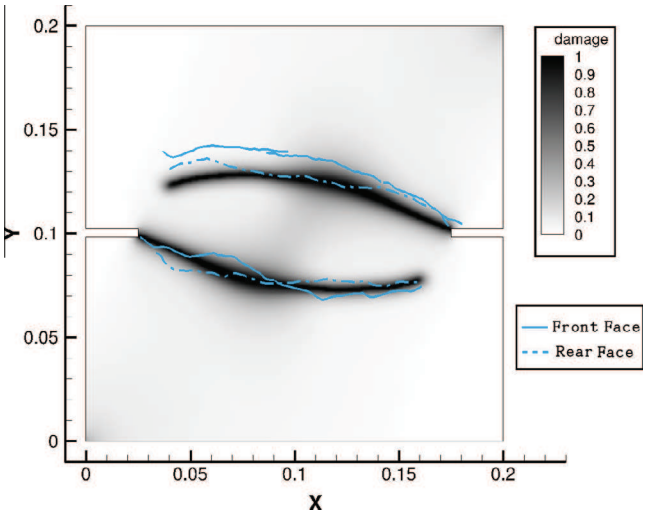

Fig. 13. Comparison between experiment and numerical simulation.

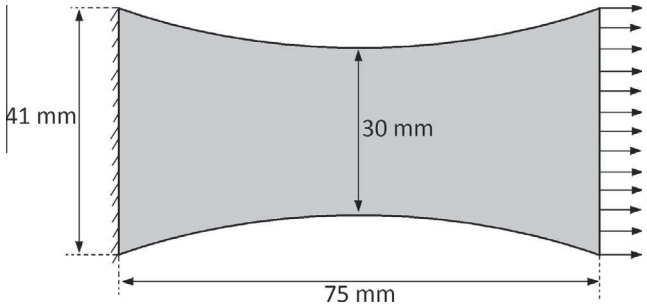

Fig. 14. Dumbell shape.

where $T1 = 268.15$ K,$T2 = 263.15$ K and $T3 = 258.15$ K. This over-determined linear system is solved with a least squares method. We obtain: $K_{I0} = 72.0$ kPa $\sqrt{\text{m}}$ and $c_T = 1.0$ kPa $\sqrt{\text{m}}$ K^{-1}. Taking law 2 ((6b)) for K_{Ic} yields the same values. Fig. 15(a) is a plot of tensile strength with temperature, on which we compare our numerical results with those of Mohamed et al.'s experiments. The identification process is successful in providing a good match between experiment and simulation. As shown Fig. 15(b), the crack topology consists of a straight crack cutting through the ice at the location of minimal section.

Law 1 (6a) and law 2 (6b) are compared in Fig. 16. Both laws yield the same results when varying grain size. A slight effect is noted with increasing porosity. However this effect is small and switching laws did not produce any visible effect when performing the subsequent simulations.

7. Numerical experiments

Icing and ice protection are complex unsteady phenomena. Icing codes typically include several modules in order to determine water droplet catch efficiency, ice growth and heat and mass transfer. A true electrothermal de-icing numerical simulation requires going through all of these steps and adding a shedding criterion. But we will not use this whole panel of modules. What we are examining is a very specific mechanism. We therefore use the possibilities offered by numerical simulation to look into the effects of varying only some parameters, all others being fixed. We consider two cases (described below). In these cases time is

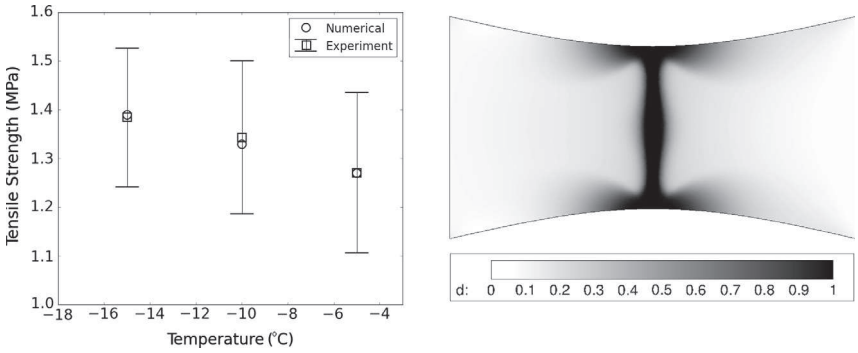

(a) Experimental and Numerical Tensile Strength. The error bars represent the standard deviation on Mohamed *et al*'s data

(b) Damage field: fractured state

Fig. 15. Tensile strength and damage field.

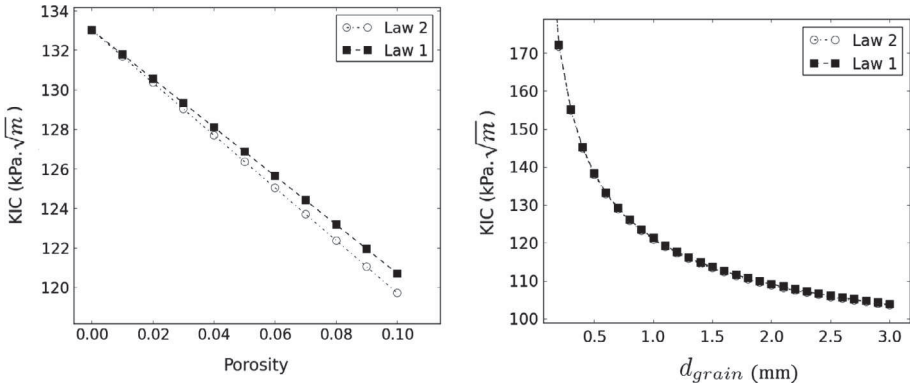

(a) Effect of porosity

(b) Effect of grain size

Fig. 16. K_{IC} as a function of grain size and porosity: Comparison between law 1 (6a) and law 2 (6b).

freezed: the ice shape is constant, the flow field is constant, and we vary the length of the water film L_f, grain size d_{grain} and porosity ϕ.

The numerical experiments are defined by using two elements:

- *An aerodynamic shape*: here a flat plate and a NACA0012 airfoil are considered.
- *A generic ice shape*: it is chosen to be shaped as a teardrop. It represents a simple form of inter-cycle ice shape. Its characteristic thickness is noted h_{ice} and is set to 3.0 mm.

The ice shape is then placed on the aerodynamic shape. In the case of the airfoil, a location that is coherent with the actual functioning of an ETIPS is chosen (not far from the parting strip). The in-house Igloo2D aerodynamics Euler solver is used to obtain the pressure distribution on the ice shape. This pressure distribution will define the Neumann boundary conditions for the crack propagation problem. Fig. 17 is a generic sketch where that illustrates the three different boundary conditions:

$$u = 0 \quad \text{on } \Gamma_u \tag{20}$$

$$\sigma \cdot n = p_{exterior} \cdot n \quad \text{on } \Gamma_{exterior} \tag{21}$$

$$\sigma \cdot n = p_{redistributed} \cdot n \quad \text{on } \Gamma_p \tag{22}$$

As explained previously, the only varying parameters will be L_f, d_{grain} and ϕ. Therefore the aerodynamic flow field is fixed once and for all for each case i.e. we do not consider any feedback process due to the eventual lifting of the ice shape, we discuss the implications of this simplification further on.

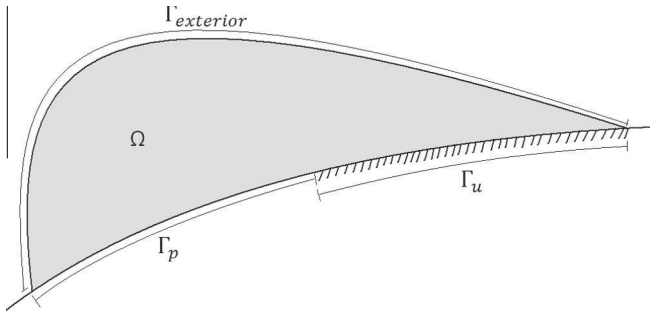

Fig. 17. Boundary curves used for specifiying boundary conditions.

Before we proceed to the actual test cases, we simplify a little further our problem. First we do not substract from the ice shape the melted region that constitutes the water film as we consider it to be negligibly small. Moreover, at the time being, surface tension effects are not taken into account. Therefore what is being considered is an idealized situation whose only goal is to help us investigate and extract what phenomena may be relevant or not.

The empirical laws for atmospheric ice were identified using experiments performed in on-ground accretion conditions (Section 6). In-flight accretion conditions are usually quite different. However, accumulation wind speed and pressure directly impact the values of grain size and porosity. Hence, the main difference between in-flight and on-ground conditions might only result in different values of grain size and porosity. Therefore, we choose

to explore different values of porosity (0–10% with 1 point increment, at fixed grain size of 0.7 mm) and grain size (0.1 mm, 0.3 mm, 0.5 mm, 0.7 mm, 1.0 mm, 1.5 mm, 2.0 mm, 2.5 mm, 3.0 mm, at fixed porosity of 3%) in order to evaluate their possible impact. Of course the impact that may or may not be observed numerically is directly linked to the empirical laws chosen and identified in Sections 3 and 6.

In typical icing conditions, ice will build up along the whole wing span. Therefore, in this case, plane strain seems to be the better choice for the two dimensional formulation of elasticity, for it corresponds to the case of a body of infinite span. However, plane stress was also used in order to gauge the impact of the 2D elasticity formulation.

To summarize two numerical experiments are defined, one which is defined by a flat plate, and the other by a NACA0012 airfoil. The experiment consists in varying L_f until fracture occurs, starting with $L_f = 0$.

7.1. Flat plate configuration

This may be the simplest case we can consider: An ice shape attached to a flat plate, illustrated Fig. 18 (not to scale). The total length of the flat plate, L_{fp} is set to 0.9 m. The length of the beveled region is $L_b = 0.05$ m and L_0 is set to 0.2 m. The thickness of the plate is $h_{fp} = 2.2$ mm. In this case $L_t = 31.225$ mm. The aerodynamic conditions are the following (see Table 2):

Fig. 20(a) shows the pressure field as given by the Euler solver, and the damage field for $\frac{L_f}{L_t} = 72\%, d_{grain} = 0.7$ mm and $\phi = 3\%$. The pressure in the water film was set to 68,000 Pa and the external pressure distribution is plotted in Fig. 19. As expected the pressure decreases when the flow goes over the ice lump. The uplifting force leads to a completely cracked state. If the ratio $\frac{L_f}{L_t}$ is too low, damage barely accumulates and fracture does not occur, as shown Fig. 20(b) ($\frac{L_f}{L_t} = 71\%, d_{grain} = 0.7$ mm and $\phi = 3\%$).

Fig. 21 represent $\frac{L_f}{L_t}$ as a function of grain size and porosity. Increasing grain size clearly has the effect of lowering the critical melted length. This is in agreement with the fact that grain size reduces fracture toughness. Variation of porosity has a lower impact in $\frac{L_f}{L_t}$. Still, the effect is visible: increasing porosity decreases the critical value of $\frac{L_f}{L_t}$.

Switching from plane strain to plane stress has the effect of reducing $\frac{L_f}{L_t}$. However the trends and conclusions remain the same as in plane strain.

7.2. Airfoil configuration

Here a more realistic case is considered: a NACA0012 airfoil on which an ice shape is attached. The aerodynamic conditions for this test case are almost the same as for the flat plate, except for the angle of attack which is set to 4°. The case is illustrated in Fig. 22 (not to scale). The ice shape starts at $x = 0.02$ m and extends over a curvilinear distance of $L_t = 0.0337$ m (see Table 3).

The pressure in the water film was set to 67,000 Pa and the external pressure distribution is plotted in Fig. 19. As in the case of the flat plate, a pressure decrease over the bump can be observed. However the pressure decrease is more pronounced. This

Table 2
Aerodynamic conditions.

Mach	P_∞ (Pa)	T_∞ (K)	α (°)
0.4	61640.0	263.15	0.0

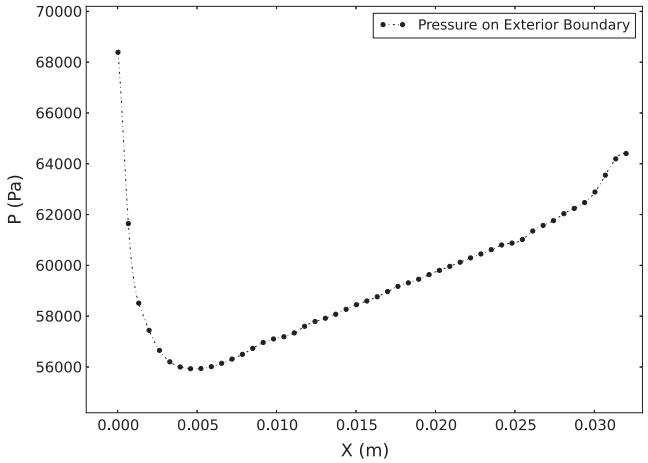

Fig. 19. Exterior pressure distribution.

leads to lower critical values of $\frac{L_f}{L_t}$. Fig. 23(b) shows the pressure field as given by the Euler solver, and the damage field for $\frac{L_f}{L_t} = 62\%, d_{grain} = 0.7$ mm and $\phi = 3\%$.

As in the case of the flat plate, increasing grain size decreases the critical value of $\frac{L_f}{L_t}$ (see Fig. 24(a)). This decrease is sharp in the range of small grain sizes and tends to stabilize for the higher values of grain size. The effect of porosity is again much slighter but still visible and has the same effect, as can be seen in Fig. 24(b). Here again, switching to plane stress decreases the values of $\frac{L_f}{L_t}$.

8. Discussion

The results of the numerical experiments show that, in both the flat plate and airfoil cases, a phenomenon of detachment before complete melting of the interface is possible. At a given critical value of $\frac{L_f}{L_t}$, the stress concentration is sufficient to enable crack nucleation and propagation over the whole thickness, therefore tearing off a certain amount of ice. The crack always nucleated from the inner tip of the melted region.

The effects of grain size and porosity on $\frac{L_f}{L_t}$ are visible. In both cases, grain size has a prominent effect for values ranging from 0.1 mm to 1.5 mm, where the critical value of $\frac{L_f}{L_t}$ is abruptly decreased when grain size increases. For values ranging from 1.5 mm to 3.0 mm the effect of grain size tends to reach a limit. As for porosity, its effect is lower but more regular. Increasing porosity decreases $\frac{L_f}{L_t}$ and it does so in a steady manner.

If we look back at Fig. 16 (b) and (a), and compare them to Figs. 21 and 24, we observe that they exhibit the same trends with

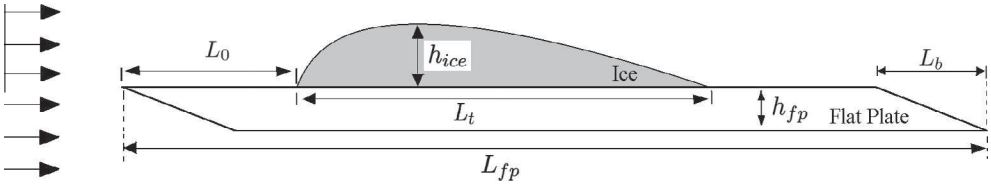

Fig. 18. Flat plate test case.

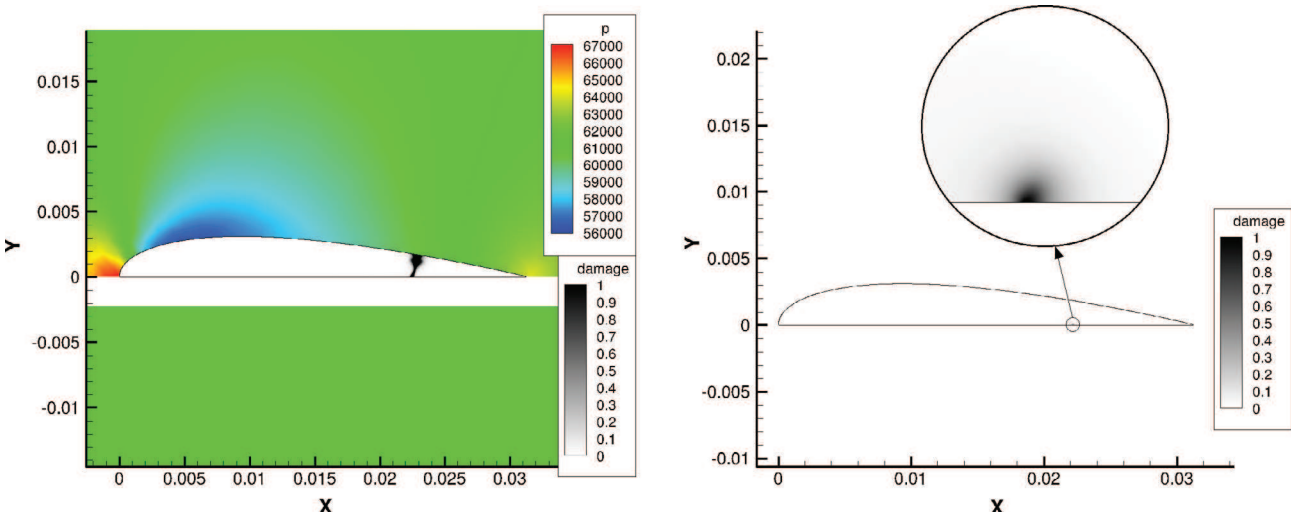

(a) Clear fractured state through the ice.

(b) No fracture if $\frac{L_f}{L_t}$ too low

Fig. 20. Pressure and damage fields.

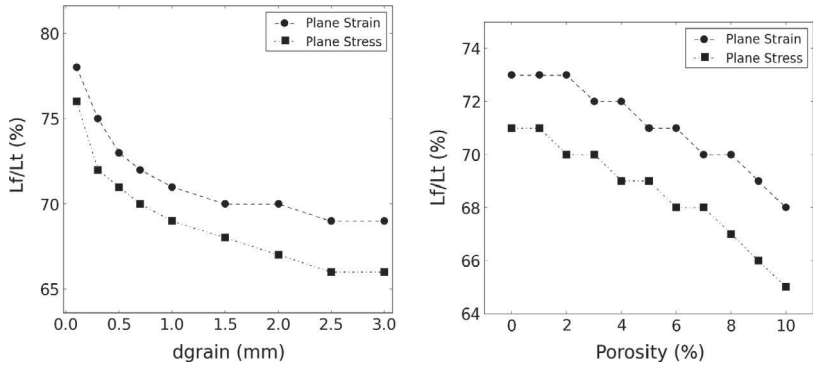

(a) Effect of grain size

(b) Effect of porosity

Fig. 21. Critical value of $\frac{L_f}{L_t}$ as a function of porosity and grain size, for both plane strain and plane stress.

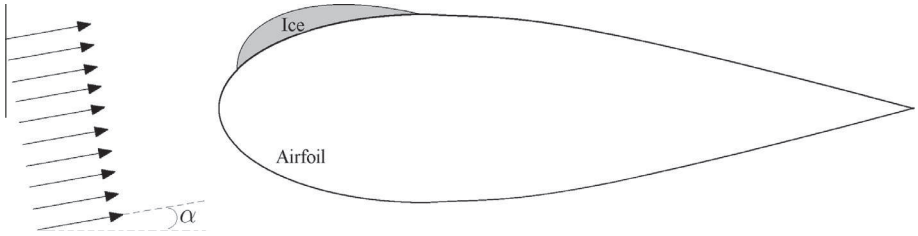

Fig. 22. Airfoil test case.

Table 3
Aerodynamic conditions.

Mach	P_∞ (Pa)	T_∞ (K)	α (°)
0.4	61640.0	263.15	2.0

respect to grain size and porosity. The mathematical model restitutes the effects of the empirical laws. One could argue that from this point of view the conclusions concerning the effect of porosity and grain size were predictable (qualitatively) and are somewhat artificial. But we should bear in mind that the problem is nonlinear. The pressure distributions could have been such that the shedding would have always occured for the same value of $\frac{L_f}{L_t}$, leaving d_{grain} and ϕ to have insignificant effects. Or, it could have been that their effects on E and K_{IC} would have not been sufficient to change the outcome of the simulations. The fact that an effect is numerically predicted means that, for this specific kind ice shedding situations, those two material parameters seem to be relevant.

We also noted that changing the two dimensional formulation from plane strain to plane stress reduces the predicted values of $\frac{L_f}{L_t}$.

However we must point out some limitations:

- In order to characterize the mechanical behavior of atmospheric ice we have used empirical relations. Although these seem to give good agreement they have their limitations. It is very

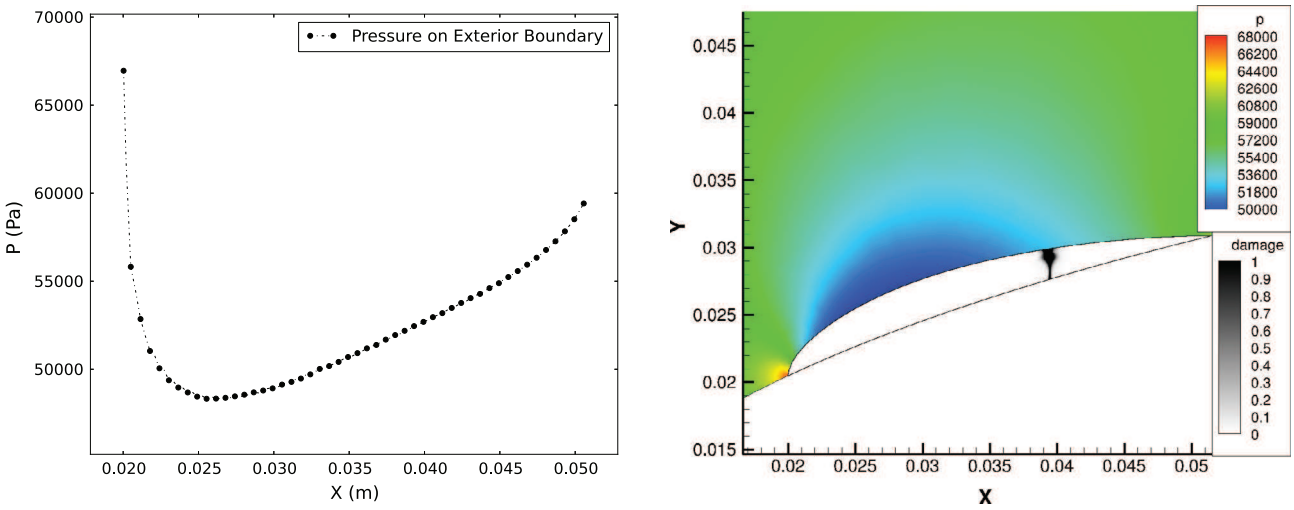

(a) Exterior pressure distribution (b) Clear fractured state through the ice

Fig. 23. Pressure distribution and damage field for the airfoil case.

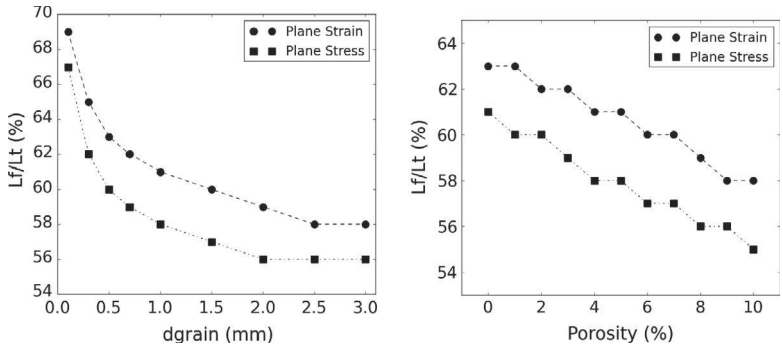

(a) Effect of grain size (b) Effect of porosity

Fig. 24. Critical value of $\frac{L_f}{L_t}$ as a function of porosity and grain size, for both plane strain and plane stress.

complicated to study the mechanical properties of atmospheric ice. Most of the time experimental results are highly scattered and no precise laws are available.

- A simplified inter-cycle ice shape was assumed.
- The ice shape may grow in time. This is not taken into account. However we do not think that this would have a large effect. The characteristic time of crack propagation is much lower than that of ice accretion (as soon as the critical ice shedding conditions are reached).
- Surface tension was not taken into account.
- Adhesion forces were not taken into account. The process may actually be a mix of fracture and purely adhesive debonding.
- Viscous flow effects such as friction were not taken into account. However the contribution of friction is negligible compared to pressure.
- In reality, a feedback process between the lifting of the ice shape and the flow field occurs. The lifting of the ice shape occurs simultaneously with a corresponding change in the flow field. And this change in flow field immediately induces a new lifting force on the ice shape. This process is not taken into account. The pressure distribution given by the first computation is considered as fixed. Still, the change in pressure distribution would lead to a higher uplifting force in this case. Therefore this should not impact the results significantly.

That being said, the results of these numerical experiments are in agreement with actual experimental observations made when testing de-icing systems in icing wind tunnels. The fact that the proposed ice shedding mechanism is the correct and/or dominant one for electro-thermal ice protection systems remains to be tested experimentally. Still, it constitutes an interesting way forward for future investigation and modeling of ice shedding.

9. Conclusion and perspectives

A possible ice detachment mechanism has been proposed and modeled using damage mechanics. Empirical relations were identified to determine the mechanical properties of atmospheric ice. This modeling strategy was first assessed on a double edge notched test case for which experimental results were available. We then considered a simple dumbell specimen in order to calibrate and identify the model parameters. With numerical results in good agreement with experimental data, two numerical experiments were defined. These simulations served to test the proposed ice shedding mechanism. They were both based on the same kind of teardrop ice shape. For both cases detachment was predicted before the whole contact length was melted. We therefore conclude that this type of shedding mechanism is relevant. Hence we will take this mechanism into account when further investigating the physical functioning of an ETIPS. These results may also be helpful in developing simplified ice shedding prediction models.

A new validation test case for the fracture mechanics model was also performed. It was based on mixed mode fracture experiments

Table 4
Numerical settings.

∅	Number of elements	Type of element	l
Dumbell	40,000	Lagrange P1	5.0×10^{-4}
Flat plate	40,000	Lagrange P1	4.0×10^{-5}
Airfoil	45,000	Lagrange P1	4.0×10^{-5}

for concrete. Very good agreement between experiment and numerical simulation was observed.

Further investigation on the mechanical properties of atmospheric ice is needed, in particular concerning aspects linked to in-flight accretion conditions. The empirical laws on which the parameter identification was based only provide a first approach. Grain size and porosity seem to play an important role in the ice shedding mechanism. Some improvement could be obtained by incorporating porosity and/or grain size directly in the constitutive law or damage model. Work in this direction has already been done by Eskandarian (poroelastic constitutive law) [7].

We have also pointed out several hypotheses that were made when simplifying the problem to obtain the numerical experiment cases. One of the main improvements we seek to add in further work is an adhesion model. This will enable us to investigate the competition between adhesive debonding and brittle failure. Ongoing work also includes the investigation of ice thickness effects.

Finally, experiments should also be conducted in order to validate this process. They would also be needed to assess the domain of validity of the chosen empirical laws for Young's modulus and fracture toughness.

Acknowledgments

This work was performed under an ANRT/Airbus C.I.F.R.E grant, we gratefully acknowledge their support. We also wish to thank Fabien Dezitter, Julien Cliquet, Matthieu Logeais, Mathieu Villedieu and Guy Burlet (Airbus) for the fruitful conversations and advice.

Appendix A. Numerical settings

All damage mechanics computations were realized with an in-house finite element code. Triangular elements were used and the meshes were generated using the open source code Triangle [19]. The numerical settings are summed up in the following table (see Table 4):

The aerodynamic computations were done with an in-house compressible Euler solver (2nd order Roe scheme (MUSCL) and implicit time stepping). Both meshes consisted of triangular elements (~35,000).

References

[1] SAE AS 5147. Thermal and fluid anti-icing systems and equipment, aircraft external surfaces. SAE subcommittee AC-9 aircraft environmental systems; July 1996.
[2] Henry R. Development of an electrothermal de-icing/anti-icing model. In: AIAA 30th meeting, Reno, NV (USA); 1991.
[3] Wright WB, Keith TG, De Witt KJ. Numerical simulation of icing, deicing and shedding. In: 29th Aerospace sciences meeting, Reno, Nevada; 1991. AIAA-91-0665.
[4] Druez J, Phan CL, Laforte JL, Nguyen DD. The adhesion of glaze and rime on aluminium electrical conductors. Trans CSME 1978–1979;5(4):215–20.
[5] Kermani M, Farzaneh M, Gagnon R. Bending strength and effective modulus of atmospheric ice. Cold Regions Sci Technol 2008;53:162–9.
[6] Mohamed AMA, Farzaneh M. An experimental study on the tensile properties of atmospheric ice. Cold Regions Sci Technol 2011;68:91–8.
[7] Eskandarian M. Ice shedding from overhead electrical lines by mechanical breaking. PhD thesis, Université du Québec a Chicoutimi; 2005.
[8] Schulson EM, Duval P. Creep and fracture of ice. 2009: Cambridge University Press; 2009.
[9] Gammon PH, Kiefte H, Clouter MJ, Denner WW. Elastic constants of artificial and natural ice samples by Brillouin spectroscopy. J Glaciol 1983;29(103):433–60.
[10] Liu HW, Miller KJ. Fracture toughness of fresh-water ice. J Glaciol 1979;22(86):135–43.
[11] Scavuzzo R, Chu M, Ananthaswamy V. Influence of aerodynamic forces in ice shedding. In: 29th Aerospace sciences meeting, Reno, Nevada; 1991. AIAA-91-0664.
[12] Zhang S, El Kerdi O, Khurram RA, Habashi WG. FEM analysis of in-flight ice break-up. Finite Elem Anal Des 2012;57:55–66.
[13] Miehe C, Hofacker M, Welschinger F. A phase field model for rate-independant crack propagation robust algorithmic implementation based on operator splits. Comput Methods Appl Mech Eng 2010:2765–78.
[14] Lemaitre J, Chaboche JL, Benallal A, Desmorat R. Mécanique des Matériaux Solides. Dunod; 2009.
[15] Griffith AA. The phenomena of rupture and flow in solids. Philos Trans Roy Soc London. Ser A 1921;221:163–78.
[16] Bourdin B, Francfort GA, Marigo JM. The variational approach to fracture. J Elast 2008;91(1–3):5–148.
[17] Nooru-Mohamed MB. Mixed-mode fracture of concrete: an experimental approach. PhD thesis, Technische Univ., Delft; 1992.
[18] Kumar S, Barai SV. Size-effect of fracture parameters for crack propagation in concrete: a comparative study. Comput Concr 2012;9(1):1–19.
[19] Shewchuk JR. Triangle: engineering a 2D quality mesh generator and Delaunay triangulator. In: Lin MC, Manocha D, editors. Applied computational geometry: towards geometric engineering. Lecture notes in computer science, vol. 1148. Springer-Verlag; 1996.